RESEARCH ARTICLE

ADVANCED OPTICAL MATERIALS
www.advopticalmat.de

Ellipticity-Controlled Exceptional Points and Cross-Polarized Phase Singularities in Multi-Layer Silicon Guided Mode Resonant Metasurfaces

Ben Goldberg, Shuang Zhang, and Mark Lawrence**

Precise control over light polarization is critical for advancing technologies in telecommunications, quantum computing, and image sensing. However, existing methods for manipulating polarization around exceptional points (EPs) in non-Hermitian systems have exclusively focused on circular polarization and work with reflected light. To address this limitation, a novel metasurface platform with high-Q resonators is developed that enables tunable control of polarization exceptional points across arbitrary ellipticity for transmitted light. This design employs orthogonally polarized guided mode resonators in a two-layer silicon metasurface, where careful tuning of the dipolar guided mode resonances (DGMRs) and layer spacing allows us to control the ellipticity of EPs. By leveraging high-quality factor resonances, strong orthogonal mode coupling over distances up to a quarter wavelength is achieved. This platform exhibits omnipolarizer behavior and the corresponding phase singularity can imprint phase shifts from 0 to 2π with small perturbations in the geometry. This approach opens new possibilities for polarization control and programmable wavefront shaping, offering significant potential for next-generation optical devices.

1. Introduction

The dynamics of open or lossy physical systems exhibit an intriguing mathematical structure. Unlike closed systems, systems that exchange energy with their environment are governed by non-Hermitian Hamiltonians, imposing far fewer constraints on the eigenmodes.[1,2] The most extreme phenomena associated with non-Hermitian physics occur near exceptional point (EP) degeneracies.[3] At an EP, not only do two or more eigenvalues of a system become degenerate, but their eigenvectors also collapse onto a single state, leaving the system with fewer stable solutions.[4] Integrated and nanoscale photonics has proven to be a very fertile testing ground for experimentally exploring these ideas. Since coupling between optical resonators and waveguides, as well as radiation leakage and absorption, can all be engineered easily, toy Hamiltonians can be manipulated in an almost arbitrary manner. EPs are of particular interest in parity-time symmetric systems as they serve as the transition point for parity-time symmetry breaking.[5–7]

Metamaterials and metasurfaces that leverage subwavelength structures to realize designer optical material properties provide a unique opportunity to exploit EP physics.[8,9] Achieving the precise balance between phase evolution and dissipation that EPs require can be challenging with natural materials but becomes straightforward with metamaterials, where properties can be tuned continuously via changes to some nanoscale geometry. Various phenomena, including unidirectional reflection, coherent perfect absorption, the non-Hermitian skin-effect, unidirectional cloaking, and ultra-responsive sensing, have been discovered via multilayer stacks of dielectrics and/or metals, coupled plasmonic particles, rings and rods, as well as coupled or multimode dielectric Mie resonators.[10–17]

Many polarization technologies involve filtering or applying a common transformation to a set of undefined or unknown states, making polarization a particularly interesting degree of freedom to embed a low dimensional eigenmode structure. It has been shown that an optical device supporting a polarization EP behaves as an omni-polarizer, where all input polarization states are pulled toward a single output polarization.[18–20] Metasurfaces are

B. Goldberg, M. Lawrence
Department of Electrical and Systems Engineering
Washington University in St. Louis
St. Louis, MO 63130, USA
E-mail: markl@wustl.edu
S. Zhang
New Cornerstone Science Laboratory
Department of Physics
University of Hong Kong
Hong Kong 999077, China
E-mail: shuzhang@hku.hk
S. Zhang
Department of Electrical and Electronic Engineering
University of Hong Kong
Hong Kong 999077, China

The ORCID identification number(s) for the author(s) of this article can be found under https://doi.org/10.1002/adom.202500731

DOI: 10.1002/adom.202500731

ideal for controlling the vector nature of light. Anisotropic dielectric or magnetic nanoparticles can be designed to selectively interact with specific components of the electric or magnetic field. By combining and/or coupling multiple nanoparticles together, every element of the complex valued Jones matrix for transmission can in principle be independently engineered. Building on important metasurface developments, including demonstrations of strong circular dichroism,[21] optical activity, and hyperbolic dispersion, polarization EPs have been observed in metasurfaces with balanced absorption anisotropy and cross-polarized transmission. Tuning metasurface parameters in the vicinity of these non-Hermitian degeneracies has revealed the presence of a cross-polarized phase singularity and a polarization phase transition, stemming from parity-time symmetry breaking, where the axis of linear birefringence rotates by 45°.[22] Far from being a mere curiosity, the fact that a state taken fully around a polarization EP will incur a topologically robust 2π phase shift has been shown to provide new degrees of freedom for wavefront shaping.[23,24] The steep gradient in phase when passing close to the singularity can also be exploited for many applications,[25,26] including sensing devices[27,28,11] and beam generation.[29] However, past research has focused purely on circularly polarized EPs.[2,30–34] Following a similar approach to the design of dielectric metasurfaces for arbitrarily polarized phase front shaping, linear and generalized elliptical polarization states have been addressed by combining circular EPs with opposite handedness.[35–38] Despite these advancements, engineering the ellipticity of polarization EPs directly has not been explored. To be clear, the devices in[30] contain only circular EPs and not elliptical or linear EPs, which is not a subtle distinction as their devices will not, for example, produce omni-polarizer action for elliptical or linear input states. During the review of our paper a study has been published demonstrating arbitrarily polarized EPs using a metasurface.[39] In that case, elliptical EPs appeared in a specific reflective diffraction order under obliquely incident illumination. Our study offers a complimentary mechanism for embedding EPs in the direct transmission through a metasurface. In recent years, there has been a growing technological interest in maximally exploiting polarization space for classical telecommunications, quantum computing, and image sensing. Therefore, omni-polarizer action tailored to an unconstrained user defined state is an exciting prospect. Moreover, we expect meta-atoms capable of directly sculpting the phase of an arbitrary polarization state to break the trade-off between metasurface phase-front resolution and polarization accuracy. In this paper, we introduce a metasurface platform based on orthogonally polarized guided mode resonators separated on different layers for tuning the ellipticity of polarization EPs from circular through to linear.

The key mechanism we will exploit to control the ellipticity of EP eigenstates is illustrated in **Figure 1**, which shows a double layer configuration. As will be explained via a coupled dipole model in Figure 1, to deviate from a circularly polarized state, a phase difference is needed between the two channels for cross-linearly polarized transmission. Mediated by the overlap of evanescent tails, nearfield interactions occur instantaneously and cannot therefore be used to manipulate the dynamics of the system. Instead, we rely on nearfield coupling alongside propagation. Specifically, by displacing meta-atoms in the propagation direction of the incoming light waves, transmission resulting from excitation of dipoles in the bottom layer and coupling back to the top layer will experience a delay due to travelling between the layers twice. On the other hand, transmission resulting from excitation of dipoles in the top layer and coupling to the bottom layer will be advanced in phase as the intervening space has been bypassed. If the size of the spacing between the two sets of resonant dipoles can be tuned by up to half of the free-space wavelength while maintaining sufficient coupling strength, any phase difference and thus EP ellipticity can be realized.

2. Results

2.1. Controlling the Ellipticity of the Exceptional Point

Each layer in a unit cell from the metasurface can be modeled as an effective dipole moment $p_{x,y} = \tilde{p}_{x,y}e^{i\omega t}$, which couples strongly to an incident radiation field $E_i e = \widetilde{E}_i e^{i\omega t}$ with radiative coupling strength g_i.[40] The geometry and material of the nanoantennas determine the resonant frequency, loss rate, and radiative coupling strength of the effective dipole moments.[41] For incident radiation that is close to resonance ($\delta_{x,y} = \omega - \omega_{x,y} \ll \omega_{x,y}$) and assuming small damping ($\gamma_{x,y} \ll \omega_{x,y}$), the transmission Jones matrix for a reciprocal metasurface is given by

$$\vec{J} = A\begin{pmatrix} g_x^2\left(\omega - \omega_y + i\gamma_y\right) & -g_x g_y G_{xy} e^{i\phi} \\ -g_x g_y G_{xy} e^{-i\phi} & g_y^2\left(\omega - \omega_x + i\gamma_x\right) \end{pmatrix} \tag{1}$$

where

$$A = \frac{i\omega\eta_0}{2d^2\left(\left(\delta_x + i\gamma_x + G_{xx}\right)\left(\delta_y + i\gamma_y + G_{yy}\right) - G_{xy}^2\right)} \tag{2}$$

G_{ij} is the nearfield coupling coefficient for i oriented radiation fields formed by j oriented dipole moments, $g_{x,y}$ is the far field coupling coefficient for fields coupling into the metasurface, and ϕ is the propagation phase imparted by the dipole layer spacing. As discussed in the context of Figure 1 above, the two off-diagonal terms have different phases because light converted from x-y polarization by the metasurface experiences a different optical path length compared to that converted from y-x polarization. Specifically, light coupled from the bottom layer back to the top layer travels between the layers twice, while light coupled from the top layer to the bottom layer never needs to travel between the layers, causing the phase difference between these two components to be $2\phi = 2n_{spacer}k_0 z_{spacer}$. It is also worth mentioning that G_{xx} and G_{yy} are encoded within the Lorentzian dipole moment and do not need to be explicitly written in (1).

The Jones vector for monochromatic light transmitted through the metasurface can be written as

$$\vec{E} = \begin{pmatrix} \tilde{E}_x(\omega) \\ \tilde{E}_y(\omega) \end{pmatrix} = \begin{pmatrix} E_x(\omega)\, e^{i\theta_x(\omega)} \\ E_y(\omega)\, e^{i\theta_y(\omega)} \end{pmatrix} \tag{3}$$

The light is circularly polarized when the phase difference between the two transmitted components is $\Delta\theta = \theta_x - \theta_y = \pm\frac{\pi}{2}$ and linearly polarized when $\Delta\theta = 0$, or an integer multiple of π. To realize elliptically polarized EPs, we must look for metasurfaces described by Jones matrices with eigenvectors that coalesce to a

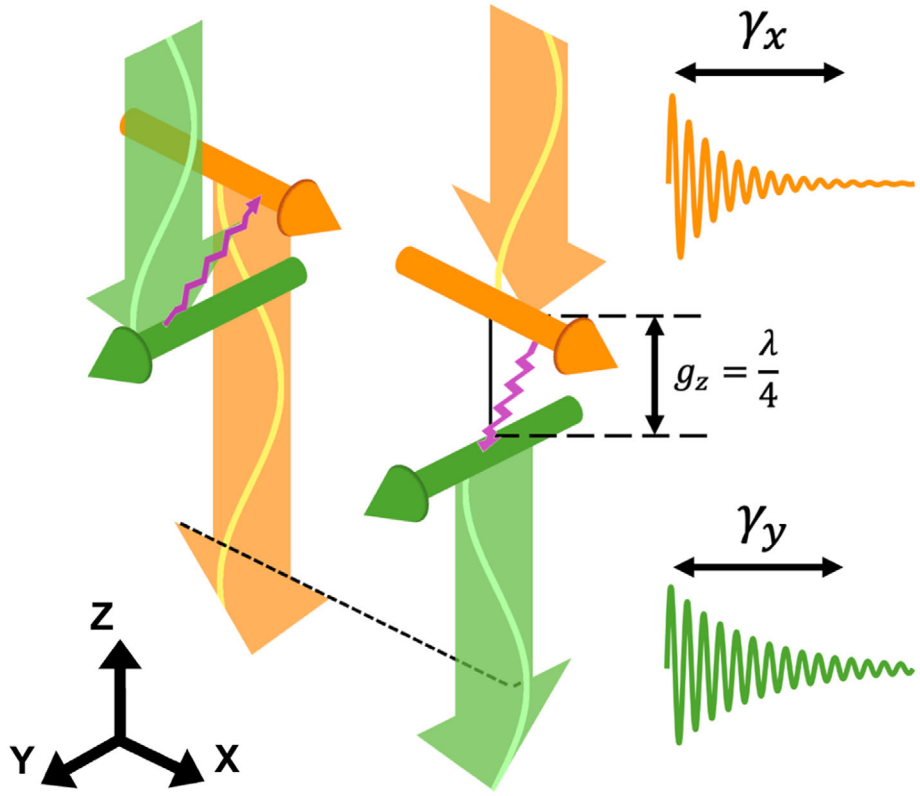

Figure 1. Summary of the key principle underpinning elliptical polarization EPs. Schematic representation of cross-polarized transmission mediated by dipole antennas with different radiative loss rates and separated onto two different layers. Reciprocal nearfield coupling between the two sets of dipoles, indicated by the purple arrows, leads to two channels for polarization conversion which have equal amplitudes. However, as y-polarized incident light travels between the two layers twice in the process of converting to x-polarization, while x-polarized incident light tunnels through to the bottom layer to become y-polarized, a phase shift develops that depends on twice the layer thickness g_z. The polarization conversion phase shift is given by $\Delta\phi = 2\phi = 4\pi\frac{g_z}{\lambda}$, meaning that $\phi = \pi/2$ which is required for a linearly polarized EP, occurs when $g_z = \frac{\lambda}{4}$. The orange decay curve represents the loss rate (γ_x) in the $\hat{x}$ direction, and the green decay curve represents the loss rate (γ_y) in the $\hat{y}$ direction. Notice that there is a nonzero difference in loss rates, $\gamma_x - \gamma_y$, between resonators of the two layers.

state having $\Delta\theta$ tunable from 0 to $\frac{\pi}{2}$. As seen in Equation (1), adding a propagation phase to the nearfield coupling terms maintains the symmetry, $t_{xy} = t_{yx}^*$, which causes the metasurface transmission eigenvalues to take the form:

$$t_{eig} = \frac{t_{xx} + t_{yy}}{2} \pm \frac{\sqrt{\left(t_{xx} - t_{yy}\right)^2 + 4\left|t_{xy}\right|^2}}{2} \tag{4}$$

After plugging the components of (1) into (4), we find that an EP degeneracy will occur at the frequency,

$$\omega = \frac{g_x^2\omega_y - g_y^2\omega_x}{g_x^2 - g_y^2} \tag{5}$$

If the coupling strength and dissipation coefficients satisfy the following relationship:

$$2g_x g_y G_{xy} = \left|g_x^2\gamma_y - g_y^2\gamma_x\right| \tag{6}$$

As has been found with two orthogonally coupled split rings,[1] choosing resonators with differing radiation losses guarantees that an exact degeneracy will be found upon sweeping G_{xy} for a fixed $g_x^2\gamma_y - g_y^2\gamma_x \neq 0$, or vice-versa, even if the resonant frequencies deviate from one another.

We note as an aside that the devices we introduce below are made from silicon and so have no absorption loss in the part of the infrared spectrum we are addressing. Lack of absorption acts to constrain $\gamma_x = g_x^2$ and $\gamma_y = g_y^2$ in Equation (1), meaning that Equation (6) can never be satisfied for finite G_{xy}. We will address this inconsistency in more detail in Section 2.4 where we will account for a background mode in our model that alters arg (t_{xx}). Equation (1) also ignores non-resonant background filtering of light that couples to the top (bottom) layer after exciting the bottom (top) layer. In our model, we assume that once a wave's electric field is rotated to be orthogonal to the dipole resonance in a particular layer the wave will no longer interact with this layer. However, extra phase and amplitude modulation will be observed if the dielectric block supports other modes outside of the band of interest, breaking the reciprocal symmetry between t_{xy} and t_{yx}. While these details influence the specific configuration for which the EP shows up, they do not affect the eigen-polarization

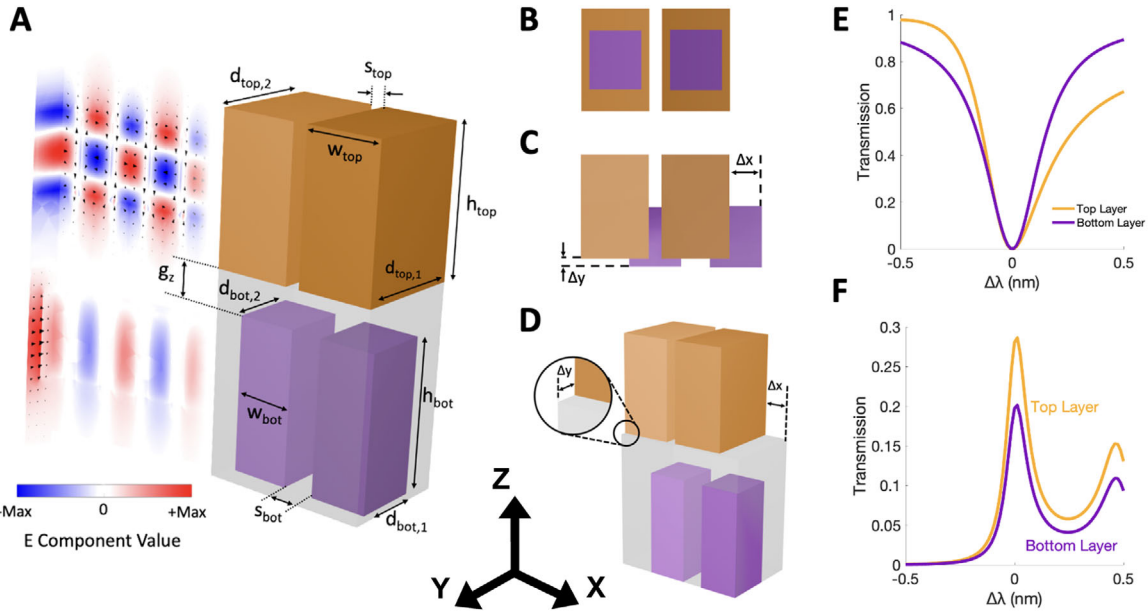

Figure 2. A) The unit cell is laid out in two layers, with each containing two rectangular prism nanostructures with slightly altered geometry. There is no coupling between resonators in different layers when the blocks are lined up. The structure shows the setup of the metasurface when the layers are aligned and there is no coupling. The colored blocks are made of silicon (n = 3.48), and the grey is the silica glass (n = 1.45) in the bottom layer. This geometry rests on a sapphire substrate with n = 1.75. The dimensions are $w_{top} = 299$ nm, $h_{top} = 575$ nm, $d_{top,1} = 450nm - \delta_{top}/2 = 444$ nm, $d_{top,2} = 450nm + \delta_{top}/2 = 456$ nm, $w_{bot} = 229$ nm, $h_{bot} = 600$ nm, $d_{bot,1} = d_{bot,0} - \delta_{bot}/2 = 260$ nm, $d_{bot,2} = d_{bot,0} + \delta_{bot}/2 = 268$ nm, $s_{top} = 56$ nm, and $s_{bot} = 126$ nm. Changing g_z adjusts the ellipticity of the EP. $g_z = 200$ nm for a linearly polarized EP. When $g_z < 200$ nm, we get a left-handed elliptically polarized EP. To fine-tune the Q-factor and precisely adjust the optical block size, we also add a refractive index difference between the two red blocks in the bottom layer. B) A top view of the metasurface when the top and bottom nanoantennas are perfectly aligned, with the silicon on the bottom layer projected on top of the silicon on the top layer. C) A top view of the unit cell when the layers are perfectly offset to maximize coupling. D) A 3D perspective view of the unit cell with layers offset to maximize coupling. The offsets are Δx = 79.5 nm and Δy = 34 nm. E) The transmission dips associated with the two guided mode resonances. We see that the dips have different widths, meaning different loss rates. This is essential for forming an exceptional point, per Equation 5–6. F) The cross-polarization curves for the resonances in both layers for the coupled states. The coupled state, depicted by the solid curves, has significant cross-polarization in both layers.

ellipticity tuning principle discussed below, and so we ignore them for now.

The eigenvector of (1) at the EP represents the EP eigenpolarization state-the only polarization remaining unchanged when passing through the metasurface. If we find the eigenvectors of our metasurface's Jones matrix in (1), we see that the eigenpolarization is a function of ϕ:

$$\frac{E_y}{E_x} = ie^{-i\phi} \tag{7}$$

From (7), we see that ϕ controls the ellipticity of the eigenpolarization. When $\phi = 0$ or π, the eigenpolarization is left-circularly polarized or right-circularly polarized respectively; but if we tune ϕ between 0 and π, we can achieve any ellipticity, with $\phi = \frac{\pi}{2}$ being linear.

Figure 1 illustrates the transmission of incident light with polarization aligned with the dipole resonators in the top layer to get them excited. By properly breaking the symmetry of the double-layer structure, the orthogonally oriented dipole antennas in the two layers are coupled with each other, leading to the near field transfer of the energy between antennas in the two layers. As mentioned earlier, there exists a phase lag between the two cross polarization transmission coefficients t_{xy} and t_{yx}, and this phase lag is proportional to the ratio between the layer spacing and the optical wavelength. When we have a layer spacing of 0 or $\frac{\lambda}{2}$, the phase is 0 and π respectively, resulting in circularly polarized light. Varying the layer spacing within this range will tune the ellipticity, achieving linearly polarized light at a spacing of $\frac{\lambda}{4}$.

However, adding such a large gap significantly reduces coupling strength. To maintain strong coupling, we needed to use modes with a very high quality factor (high-Q). To meet this requirement, we designed our structure to exploit guided mode resonance from a nanoantenna metasurface since this structure can be tuned to arbitrarily high-Q.[42,43]

2.2. Unit Cell Design

In this section, we discuss the design of the metasurface unit cell and how it leads to two coupled high-Q guided mode resonators. As shown in **Figure** 2A, the metasurface is composed of two layers of silicon guided mode resonators with the top and bottom layer hosting x- and y- polarized guided mode resonance, respectively.

Each individual silicon nano-block supports a Mie-like resonance. The guided mode resonance is formed by the electromagnetic coupling between adjacent nanostructures. The unit cell of the metasurface consists of four blocks, two in each layer. The two adjacent blocks within each layer have slightly different block

widths in the y-direction. The coupling between the two neighboring blocks forms a bright mode of low Q and a dark mode of high Q. Here we focus on the dark mode, where the emissions from adjacent blocks are out of phase. To locate the EP, precise adjustments to the Q of the dark mode of each layer are necessary. In general, the emitted radiation of the dark mode is proportional to the difference in the dipole strength between the adjacent blocks, which in turn is proportional to the difference in block sizes. Therefore, in principle, by adjusting the size difference between adjacent blocks, one can precisely tune the loss of the nanostructure, thereby adjusting the quality factor (Q). Alternatively, modifying the refractive index can serve as a more reliable way of tuning the Q since it does not require nanometer-level changes in our numerical model.

By carefully tailoring the geometry of the antennas, the two dark modes supported by the two layers can be designed to resonate at the same frequency. Further, the resonant frequencies should be far away from background modes, because background modes can inhibit transmission due to destructive interference.

It is important to introduce coupling between the two dark modes in the top and bottom layers to allow the first mode to excite the second, and vice-versa. This occurs when several conditions are met, the most important of which being that the modes resonate at the same frequency and have overlapping field components (e.g. E_x field overlaps in both modes). For our metasurface, the alignment in the XY-plane of the two layers can be adjusted to maximize E_x field overlap. The need for an in-plane relative shift between the metasurfaces tracks the strength of 2D inversion symmetry breaking, meaning that when there is significant inter-layer coupling the bi-layer metasurface is 3D chiral. Interestingly, however, the ellipticity of the EP depends on the precise layer separation rather than inversion symmetry, and so a structure with a linear EP is just as chiral as one supporting an elliptical EP. Unfortunately, the evanescent decay of optical field strength outside of the silicon blocks inevitably causes the maximum overlap between modes lying in different layers to be very small when targeting larger cross-polarized phase delays. EPs can still be observed using smaller coupling coefficients, but the non-Hermitian behavior will become more fragile. For an omni-polarizer based on sufficiently weak coupling, the efficiency at which light is converted to the EP state after illuminating with its orthogonal polarization may be negligible. To counteract this problem, we exploit the fact that the cross-polarized transmission depends on the ratio between the coupling rate and the resonator damping rates. Minimizing radiation loss to achieve Q factors in the thousands allows us to realize strong polarization conversion even for large layer separations. To achieve large individual Q factors as well as a precise difference between the Q factors, we adjusted the difference in depth of the blocks, i.e. the dimension in the y-direction, until the system approaches the EP. Linearly and elliptically polarized EPs are triangulated via purely geometric tuning in Figure S2 (Supporting Information). However, to analyze the parameter space in detail while avoiding numerical instabilities arising from making very fine geometric changes, we choose to instead introduce a small refractive index bias Δn between adjacent silicon blocks in the bottom layer, as labelled in the inset of Figure 3A, to induce an effective difference in the optical size of adjacent blocks. After these adjustments, the Q factors in the top and bottom layers were 7170 and 17800, respectively.

Finally, the separation between the two layers is controlled to adjust φ, providing tunability of the ellipticity of the EP. Figure 2C,D shows the unit cell of this double-layer metasurface when the layers are offset to maximize coupling, with Figure 2C showing a top view and Figure 2D providing the 3D perspective view. Figure 2E illustrates the independent cross-polarized transmission for each layer, showing that it reaches a maximum at the mode's resonant frequency.

2.3. Polarization Eigen-Transmission

After obtaining the transmission Jones matrix, one can analyze the eigen polarization states for transmission. Since the Jones matrix is a 2x2 matrix, it has two eigenvalues and eigenvectors given by

$$\bar{\bar{J}}\ (\omega)\ \vec{E}\ (\omega) = \lambda\ (\omega)\ \vec{E}\ (\omega) \tag{8}$$

where $\vec{E}$ is the polarization eigenvector of the metasurface and λ is the eigenvalue, representing the transmission coefficient when the polarization state of the incident light coincides with the eigenvectors. It is helpful to visualize the eigen-polarization states in terms of their orientation and ellipticity, which can be mapped onto a Poincaré sphere, where the longitude lines represent varying orientations, and latitude lines represent varying ellipticities, with the circular polarizations located at the north and south poles. **Figure** 3A,B shows the Poincaré sphere for an elliptically polarized EP and a near-linearly polarized EP, respectively. In terms of tuning the EP polarization, the most significant difference between the meta-structure simulated in Figure 3A and that modelled in Figure 3B is the layer spacing and therefore total thickness, $h_{total} = 1325$ for the elliptical EP and $h_{total} = 1375$ for the linear EP. However, as the resonances and critical coupling condition in question are sensitive to the layer spacing, we made slight geometric changes in order to spectrally and spatially align the modes in each layer, for each layer spacing. In particular, we have modified w_{bot} and $d_{bot,\,0}$, to spectrally align the resonances, and δ_{bot} and δ_{top}, to control the difference in Q-factors. Each color of dots on the Poincarè sphere represents a different Δn value, which is the difference in refractive index between adjacent silicon blocks in the bottom layer. Different dots of the same color represent the eigenpolarizations over varying wavelengths. As the layer spacing is decreased (i.e. the total height of the metasurface, h_{total}, is decreased), it is observed that the polarization of the EP shifts from linear to elliptical. Figure S3 (Supporting Information) also demonstrates that the layer spacing provides continuous control over the EP ellipticity.

The eigen-transmission spectrum in **Figure** 4B shows how the eigenvalues change for varying frequencies. As the Q-factor changes, the eigentransmission spectrum shifts from crossing, merely touching at the EP, to not touching.

2.4. Dipole Model Simulations

The dipole model given by (1) and (2) explains the basic principle of how elliptically polarized EPs can arise in ideal bi-layer

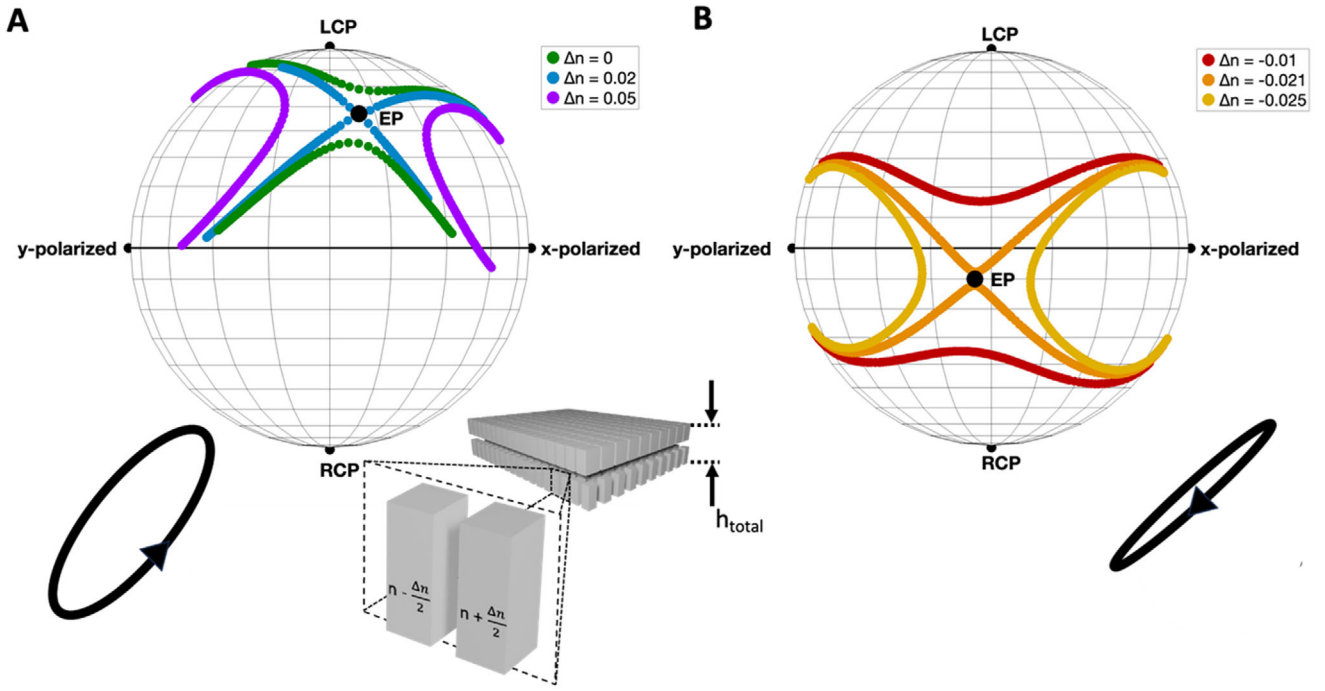

Figure 3. Poincare sphere for EPs found at different ellipticities. A) h_{total} = 1325 nm produces an elliptical EP with ellipticity 20.26°. Dimensions as defined in the caption of Figure 2 are w_{bot} = 205 nm, $d_{bot,0}$ = 264 nm, δ_{bot} = 26 nm, δ_{top} = 24 nm. All data in panel A has been calculated with the same geometry, with the different colors corresponding to different refractive index perturbations in the bottom metasurface layer, as defined by the inset. The EP is about halfway between a true linear and true circular polarization. The Δn = 0.02 geometry is closest to the EP. B) h_{total} = 1375 nm produces an EP that's near linear with an orientation of −47.4°. Dimensions as defined in the caption of Figure 2 are w_{bot} = 229 nm, $d_{bot,0}$ = 264 nm, δ_{bot} = 8 nm, δ_{top} = 12 nm. All data in panel B has been calculated with the same geometry, with the different colors corresponding to different refractive index perturbations in the bottom metasurface layer, as defined by the inset. The Δn = −0.021 geometry is the closest to the EP.

metasurfaces; however, it does not map exactly on to our numerical results for two reasons. First, there is no absorption loss in the dielectric metasurface, meaning $g_{x,y}^2 = \gamma_{x,y}$. This forces the diagonal elements in the Jones transmission matrix to be identical, meaning that polarization transformations will be governed by a Hermitian matrix with orthogonal eigenstates. Second, as will be shown below, the EP is not positioned close to the resonant frequency of the broadband mode in our numerical eigentransmission spectra. While the dipole model predicts that an EP should be found for any pair of resonant frequencies, including the same frequency, given the right difference in loss rates, our dielectric metasurface seems to require a spectral shift between the higher and lower Q modes. It turns out that non-idealities in the form of a complex valued background transmission for just one of the polarization channels account for both differences. Conveniently, a broadband anisotropic background circumvents the need for material loss without changing the relationship between EP polarization and layer separation.

Although the background response is composed of many Mie resonances in both layers, without loss of generality we can model the non-ideal background behavior by adding a single x-polarized broadband resonance to the dipole model above. Specifically, we add the following term to t_{xx}:

$$\frac{g_b^2}{\omega - \omega_b + i\gamma_b} \tag{9}$$

By adjusting the parameters for G_{xy}, g_x, g_y, ω_x, ω_y and setting $\phi = \frac{\pi}{2}$ for a layer spacing of $\frac{\lambda}{4}$, we can reproduce similar eigentransmission plots and Poincaré sphere plots as those in Figures 4 and 5.

By taking into account the background response, the EP calculated by the dipole model simulation is depicted in Figure S1A (Supporting Information). It can also be observed in the eigentransmission spectra in Figure S1B,C (Supporting Information), where the EP is located on the right side of the dip where the two curves almost touch. The asymmetry of the EP's location with respect to the eigentransmission spectra dip is also shown in Figure 4B. Interestingly, we find that after being superimposed onto an anisotropic partially reflecting background, scattering from coupled absorption-free resonators shares the same non-Hermitian physics as a pair of absorptive resonators. Essentially, interference between the resonant and background scattering gives control over the difference in imaginary parts for the diagonal elements of the Jones matrix. That insight may lead to highly efficient non-Hermitian polarizers.

2.5. Phase Gradient Topology

The most exotic features of systems with a non-Hermitian degeneracy show up when illuminating them with the orthogonal state to the EP (i.e. the Jordan vector), both at the EP wavelength and in the parametric neighborhood surrounding it. We expect to find

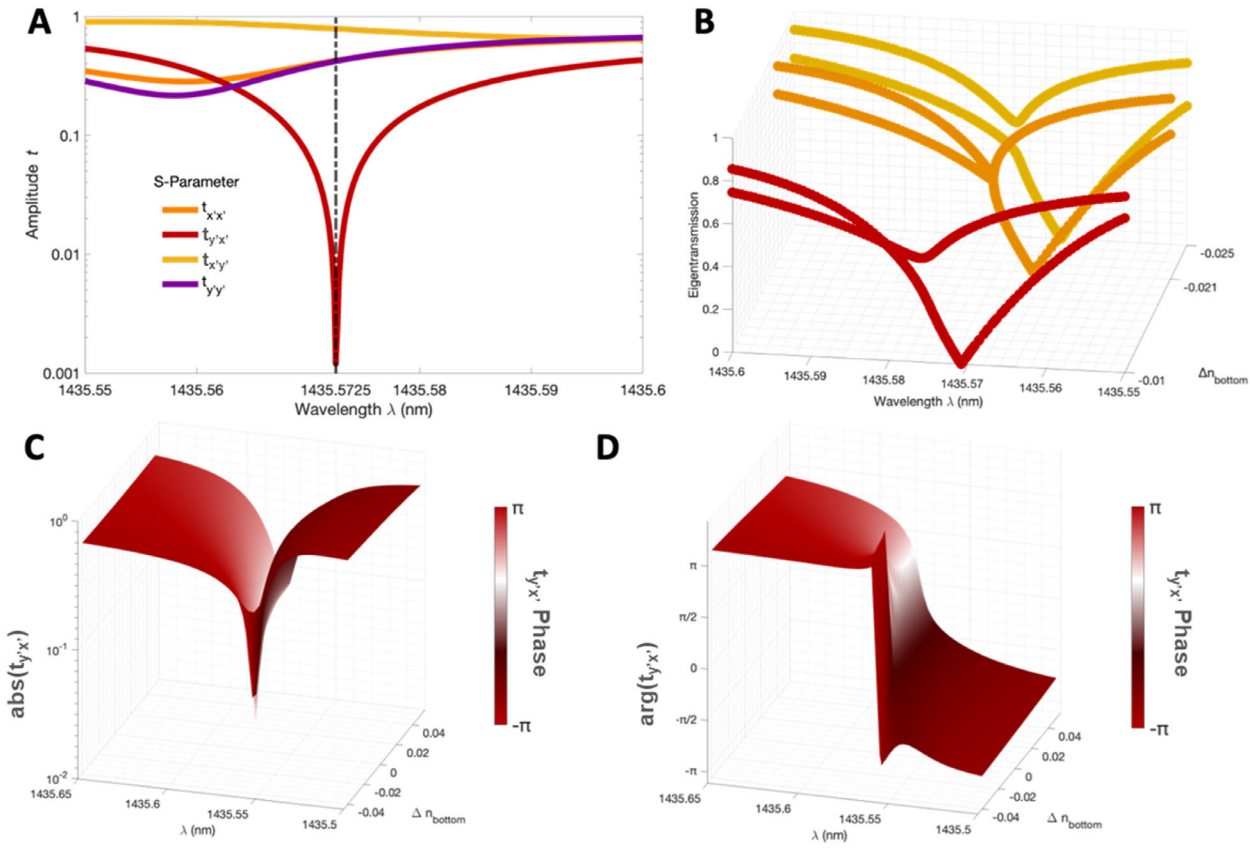

Figure 4. A) The magnitude of the four Jones matrix components, in an orthonormal basis including the EP polarization state, plotted on log-scale over the wavelength range around the EP. Notice that the $t_{y'x'}$ component reaches near-zero for $\lambda \approx 1435.5725$ nm. B) The eigentransmission spectra for geometrically identical metasurfaces with three different refractive index differences in the bottom layer near the EP. The eigentransmission spectra for structures where $\Delta n = -0.01$, $\Delta n = -0.021$, and $\Delta n = -0.025$ are shown. These represent Q-factor greater than, near, and less than the exceptional point. C) The Jones matrix parameters are rotated from an XY basis to the basis of the EP, which is rotated −47.4° off the positive x-axis. This transformation highlights the nature of the metasurface's re-polarization. Here we see the magnitude of the $t_{y'x'}$ component plotted over a wavelength and Δn_{bottom} (refractive index difference) range near the EP. The color represents the phase at each point of the parameter space. D) The phase of the $t_{x'y'}$ component plotted over a wavelength and Δn_{bottom} (refractive index difference) range near the EP. The color represents the phase at each point of the parameter space. All simulations in this figure used the geometry from Figure 3B, with dimensions given in the caption of Figure 3.

strong one-way polarization conversion as well as a topologically robust phase winding for paths looping around the singularity. Beyond the fundamental interest of endowing arbitrary polarization states with topological properties, such phase winding has been shown to represent a powerful tool for wave shaping. We simulated the metasurface to obtain a series of Jones matrices at frequencies near our linear EP. For the metasurface described in Figure 3B, since the eigen polarization state of the EP for our designed metasurface is approximately linearly polarized at an angle of −47.4° with respect to the y-direction, we calculate the Jones matrix in the basis formed by the eigenvector (x') and Jordan vector (y') via unitary transformation, which we will refer to as $\bar{\bar{J}}_{EP}$.

We plotted the four components of $\bar{\bar{J}}_{EP}$, the Jones matrix in an orthonormal basis including the EP polarization state, over a wavelength range swept across the EP in Figure 4A. We find that the $t_{y'x'}$ component, corresponding to conversion from the EP polarization state to the Jordan vector, reached zero at the EP wavelength, while the $t_{x'y'}$ component, corresponding to conversion from the Jordan vector to the EP polarization state, remained ≈ 0.8. This indicates that a high amount of y' polarized light is rotated to x' polarized light, while almost no x' polarized light is converted to y' polarized light. Figure 4B shows the eigentransmission spectra corresponding to all three curves on the Poincaré sphere in Figure 3B.

We further analyzed the $t_{x'y'}$ component by measuring it over a wavelength and refractive index sweep. As described in Section 2.2, the quality factor (Q) of the bottom layer is directly related to the difference in size of the adjacent blocks. Figure 4A shows the four Jones matrix components plotted over a wavelength range around the EP for $\Delta n = -0.021$. Figure 4B shows the eigentransmission spectra for wavelengths around the EP, and three refractive index differences, $\Delta n = -0.01$, $\Delta n = -0.021$, and $\Delta n = -0.025$. Figure 4C shows on log-scale how the magnitude of $t_{x'y'}$ changes for continuously varying wavelengths and Δn. A sharp drop is seen at the wavelength and Δn of the EP. The color of the surface shows the phase of $t_{x'y'}$. Figure 4D shows the phase of $t_{x'y'}$ over the same wavelength and Δn range, and the color also represents the phase, revealing the expected topological phase singularity.

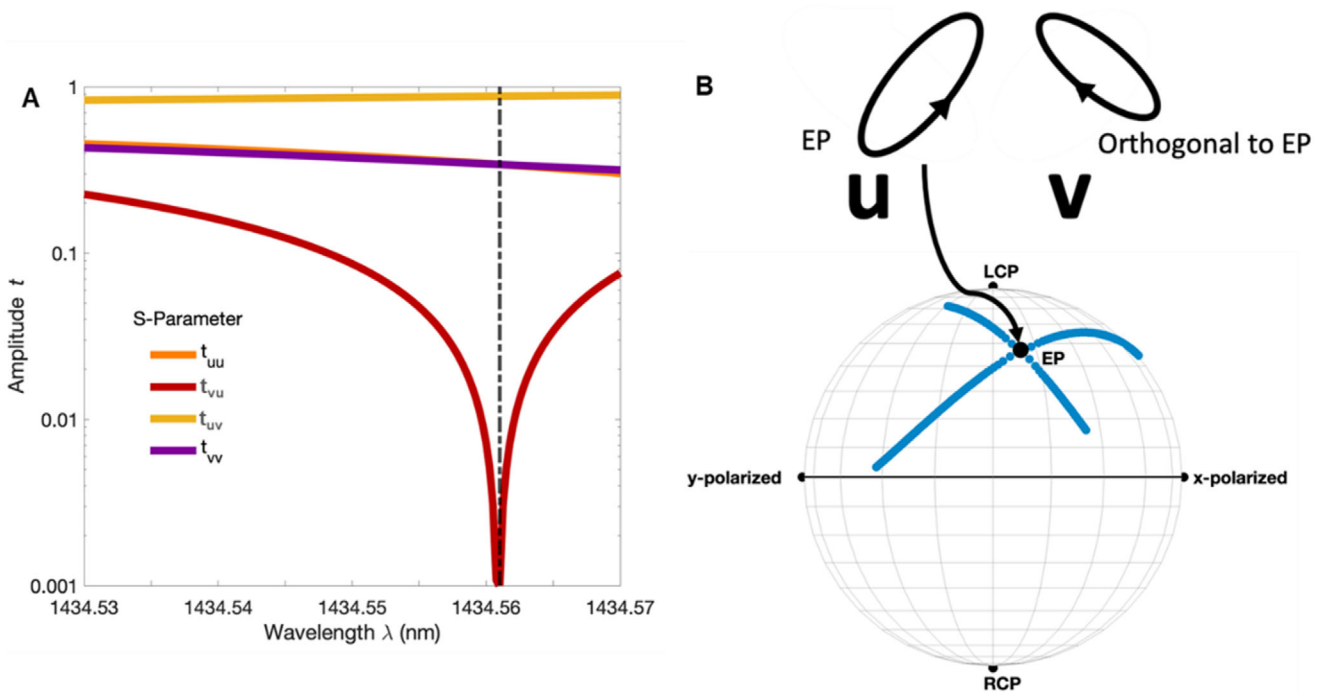

Figure 5. One way polarization conversion from bi-layer metasurface with $h_{total} = 1300$ nm. The Jones matrix parameters when rotated from an XY basis into the UV basis. u is the polarization at the EP, and v is the polarization orthogonal to the EP. Plotting these components highlights the nature of the metasurface's polarization conversion. At the wavelength of the EP, the t_{vu} component drops to zero, while the t_{uv} component is near one, indicating a large amount of light is converted from the v state to the u state. All simulations in this figure used the geometry from Figure 3A, with dimensions given in the caption of Figure 3.

The same phase gradient topology can be observed for an EP with intermediate ellipticity between a circular state and linear state. Consider the structure from Figure 3A which has a smaller layer spacing compared to the metasurface in Figures 3B and 4, meaning that the cross-polarization phase difference is reduced. After transforming the Jones matrix, $\bar{\bar{J}}_{xy}$ from an XY basis into the basis of the new EP, we plot the components of the elliptically polarized Jones matrix, $\bar{\bar{J}}_{EP}$, as a function of wavelength close to the EP in **Figure 5**. From this plot we clearly see how the components of our new $\bar{\bar{J}}_{uv}$ behave very similar to the components of $\bar{\bar{J}}_{x'y'}$ for the linearly polarized EP, again revealing a zero in the conversion efficiency away from the EP polarization and a corresponding topological phase winding.

3. Discussion

In this work, we have introduced and numerically demonstrated a scheme for controlling the ellipticity of polarization EPs using bi-layer guided mode resonant metasurfaces. We show via a coupled dipole model that the key to elliptical EPs is precisely controlling nearfield interactions between perpendicular dipole antennas that have a significant out-of-plane separation. A finite propagation-based phase delay between the layers shows up in the complex valued off-diagonal components of the Jones matrix as well as the phase difference between orthogonal components of the Eigenvectors. Given that coupling mediated by evanescent fields drops exponentially with separation, it seems that the strength of non-Hermitian anisotropy must drop as the targeted coupling phase increases. Guided mode resonances provide the solution to this trade-off. By working with high quality factor resonances, modes with weak spatial overlap can still hybridize efficiently thanks to the extended interaction time. As a proof-of-principle, we selected two distinct layer spacings and tailored the quality factor differences and coupling strengths in each case to reach the exceptional points. With these designs we observed omni-polarizer action for both an elliptical state and an almost linear polarization state. By exploring the parameter space around the exceptional points of metasurfaces with different layer spacings, we confirmed the existence of cross-polarized phase singularities in linear and generalized elliptical polarization bases. The ability these singularities provide to imprint any transmitted phase across 0–2π onto any desired polarization state via a single subwavelength meta-molecule will find important applications in wavefront shaping. Interestingly, we observe highly non-Hermitian behavior in a system without absorption. From our dipole model we conclude that this is only possible after introducing a third broad background mode, which could serve as a guide to low-loss exceptional point device engineering. Lastly, as well as amplifying the coupling strength between remote dipole antennas, highly resonant non-Hermitian anisotropy may open the door to efficiently programmable polarization control.

4. Materials and Methods

Numerical simulations were performed using the finite element software COMSOL Multiphysics. All metasurfaces were modelled as infinitely periodic by applying periodic boundary conditions in the x and y directions. Port boundary conditions with x and y polarized electric fields were applied in the z direction in order to calculate the four complex valued and wavelength dependent components of Jones matrices in the x-y basis for normally incident transmission. The response to other polarization states was determined by applying unitary transformations to the linear x-y basis Jones matrices. All materials were modelled as lossless and dispersion less dielectrics.

5. Proposed Fabrication Process

The feasibility of our proposed scheme is bolstered by the fact that bilayer metasurfaces have been fabricated and characterized by a number of research groups.[44,45] An example fabrication procedure for the specific meta-structure shown in Figure 2 would begin with a silicon on sapphire wafer. The bottom layer metasurface could be patterned via electron-beam lithography followed by reactive ion etching. Plasma-enhanced chemical vapor deposition or atomic layer deposition would then be used to deposit the silica spacer layer and then a second silicon layer. Finally, electron beam lithography would be repeated to fabricate the top metasurface layer. Precise alignment between the two silicon layers is crucial and can be achieved by including alignment markers during the first lithography step.

Supporting Information

Supporting Information is available from the Wiley Online Library or from the author.

Acknowledgements

The authors thank the National Science Foundation (NSF) under grant no. CCF-2416375, the New Cornerstone Science Foundation, and the Research Grants Council of Hong Kong (STG3/E-704/23-N, AoE/P-701/20, 17309021), for financial support.

Conflict of Interest

The authors declare no conflict of interest.

Author Contributions

M.L. and S.Z. conceived the idea, with M.L. designing the research. B.G. performed numerical simulations and analytical calculations. M.L. supervised the work. M.L. and B.G. co-wrote the manuscript. All authors contributed to the discussion of the results and provided comments on the manuscript.

Data Availability Statement

The data that supports the findings of this study are available from the corresponding author upon reasonable request.

Keywords

metasurfaces, non-Hermitian optics, polarization exceptional points

Received: March 5, 2025
Revised: June 4, 2025
Published online: July 14, 2025

[1] Y. Ashida, G. Zongping, M. Ueda, *Adv. Phys.* **2020**, *69*, 249.
[2] S. H. Park, et al., *Nanophotonics* **2020**, *9*, 1031.
[3] W. D. Heiss, *J. Phys. A Math. Gen.* **2004**, *37*, 2455.
[4] E. M. Graefe, U. Günther, H. J. Korsch, A. E. Niederle, *J. Phys. A Math. Theor.* **2008**, *41*, 255206.
[5] M.-A. Miri, A. Alù, *Science* **2019**, *363*, aar7709.
[6] W. D. Heiss, *J. Phys. A Math. Theor.* **2012**, *45*, 444016.
[7] S. Klaiman, U. Günther, N. Moiseyev, *Phys. Rev. Lett.* **2008**, *101*, 80402.
[8] X. Wu, X. Zhao, Y. Lin, F. Lin, Z. Fang, *ACS Photonics* **2024**, *11*, 2054.
[9] L. Feng, R. El-Ganainy, L. Ge, *Nat. Photonics* **2017**, *11*, 752.
[10] C. Zeng, Y. Sun, G. Li, Y. Li, H. Jiang, Y. Yang, H. Chen, *Opt. Express* **2019**, *27*, 27562.
[11] W. Chen, Ş. Kaya Özdemir, G. Zhao, J. Wiersig, L. Yang, *Nature* **2017**, *548*, 192.
[12] B.o Zhen, C. W. Hsu, Y. Igarashi, L. Lu, I. Kaminer, A. Pick, S.-L. Chua, J. D. Joannopoulos, M. Soljacic, *Nature* **2015**, *525*, 354.
[13] A. E. Miroshnichenko, A. B. Evlyukhin, Y. S. Kivshar, B. N. Chichkov, *ACS Photonics* **2015**, *2*, 1423.
[14] S. Longhi, *Phys Rev A* **2010**, *82*, 31801.
[15] S. Yao, Z. Wang, *Phys. Rev. Lett.* **2018**, *121*, 86803.
[16] Z. Lin, H. Ramezani, T. Eichelkraut, T. Kottos, H. Cao, D. N. Christodoulides, *Phys. Rev. Lett.* **2011**, *106*, 213901.
[17] Y. D. Chong, L. Ge, H. Cao, A. D. Stone, *Phys. Rev. Lett.* **2010**, *105*, 53901.
[18] D. Oh, et al., *Nanophotonics* **2024**, *13*, 4409.
[19] A. U. Hassan, B. Zhen, M. Soljačić, M. Khajavikhan, D. N. Christodoulides, *Phys. Rev. Lett.* **2017**, *118*, 93002.
[20] J. Fatome, S. Pitois, P. Morin, E. Assémat, D. Sugny, A. Picozzi, H. R. Jauslin, G. Millot, V. V. Kozlov, S. Wabnitz, *Sci. Rep.* **2012**, *2*, 938.
[21] C. Wang, R. Wang, X. Cheng, X. Hu, C. Wang, *ACS Nano* **2024**, *18*, 18922.
[22] T. T. Sergeev, A. A. Zyablovsky, E. S. Andrianov, Y. E. Lozovik, *Quantum* **2023**, *7*, 982.
[23] M. V. Berry, *Proc. Royal Soc. London. A. Math. Phys. Sci.* **1997**, *392*, 45.
[24] J. W. Yoon, Y. Choi, C. Hahn, G. Kim, S. H.o Song, K.i-Y. Yang, J. Y. Lee, Y. Kim, C. S. Lee, J. K. Shin, H.-S. Lee, P. Berini, *Nature* **2018**, *562*, 86.
[25] F. Ding, Y. Deng, C. Meng, P. C. V. Thrane, S. I. Bozhevolnyi, *Sci. Adv.* **2025**, *10*, adl4661.
[26] N. Yu, P. Genevet, M. A. Kats, F. Aieta, J.-P. Tetienne, F. Capasso, Z. Gaburro, *Science* **2011**, *334*, 333.
[27] F. Yesilkoy, R. A. Terborg, J. Pello, A. A. Belushkin, Y. Jahani, V. Pruneri, H. Altug, *Light Sci. Appl.* **2018**, *7*, 17152.
[28] V. G. Kravets, F. Schedin, R. Jalil, L. Britnell, R. V. Gorbachev, D. Ansell, B. Thackray, K. S. Novoselov, A. K. Geim, A. V. Kabashin, A. N. Grigorenko, *Nat. Mater.* **2013**, *12*, 304.
[29] H.o M. Leung, W. Gao, R. Zhang, Q. Zhao, X. Wang, C. T. Chan, J. Li, W. Y. Tam, *Opt. Express* **2020**, *28*, 503.
[30] Q. Song, M. Odeh, J. Zúñiga-Pérez, B. Kanté, P. Genevet, *Science* **2011**, *373*, 1133.
[31] M. Lawrence, *Doctoral Dissertation*, University of Birmingham, Birmingham **2015**.

[32] W. He, S. Wan, Y. Zuo, S. Hu, Z. Ren, Z. Yu, D. Yang, X. '. Cheng, K. Xia, Y. Hu, H. Jing, T. Jiang, *Phys. Rev. Lett.* **2025**, *134*, 106901.
[33] Z. Yu, W. He, S. Hu, Z. Ren, S. Wan, X. '. Cheng, Y. Hu, T. Jiang, *Adv. Sci.* **2024**, *11*, 2402615.
[34] H. Li, G. Yang, A. Jiang, M. Ni, Q. Jia, F. Cao, J. Zhang, B. Lyu, D. Liu, J. Shi, *Photonics Res.* **2024**, *12*, 2863.
[35] Z. Yang, P.-S. Huang, Y.-T. Lin, H. Qin, J. Zuniga-Pérez, Y. Shi, Z. Wang, X. Cheng, M.-C. Tang, S. Han, B. Kanté, B.o Li, P. C. Wu, P. Genevet, Q. Song, *Nat. Commun.* **2024**, *15*, 232.
[36] Q. Song, S. Khadir, S. Vézian, B. Damilano, P. D. Mierry, S. Chenot, V. Brandli, P. Genevet, *Sci. Adv.* **2024**, *7*, abe1112.
[37] J. P. Balthasar Mueller, N. A. Rubin, R. C. Devlin, B. Groever, F. Capasso, *Phys. Rev. Lett.* **2017**, *118*, 113901.
[38] S. Wang, Z.-L. Deng, Y. Wang, Q. Zhou, X. Wang, Y. Cao, B.-O. Guan, S. Xiao, X. Li, *Light Sci. Appl.* **2021**, *10*, 24.
[39] H. Qin, Z. Yang, P.-S. Huang, X. Mu, S.-H. Huang, Y. Shi, W. Zhao, B. Li, J. Zhou, J. Jesús-Pérez, P. Genevet, P. C. Wu, Q. Song, *Nat. Commun.* **2025**, *16*, 2656.
[40] M. Lawrence, N. Xu, X. Zhang, L. Cong, J. Han, W. Zhang, S. Zhang, *Phys. Rev. Lett.* **2014**, *113*, 93901.
[41] A. Guo, G. J. Salamo, D. Duchesne, R. Morandotti, M. Volatier-Ravat, V. Aimez, G. A. Siviloglou, D. N. Christodoulides, *Phys. Rev. Lett.* **2009**, *103*, 93902.
[42] M. Lawrence, D. R. Barton, J. Dixon, J.-H. Song, J. van de Groep, M. L. Brongersma, J. A. Dionne, *Nat. Nanotechnol.* **2020**, *15*, 956.
[43] L. Lin, J. Hu, S. Dagli, J. A. Dionne, M. Lawrence, *Nano Lett.* **2023**, *23*, 1355.
[44] L. Deng, Z. Li, Z. Zhou, Z. He, Y. Zeng, G. Zheng, S. Yu, *Adv. Opt. Mater.* **2022**, *10*, 2102179.
[45] A. H. Dorrah, J.-S. Park, A. Palmieri, F. Capasso, *Nat. Commun.* **2025**, *16*, 3126.